LETTER | MAY 22 2026

Defects, corrugation, and temperature govern rarefied-air drag on graphene coatings

Samuel Cajahuaringa ; Davide Bidoggia ; Maria Peressi ; Antimo Marrazzo

Physics of Fluids 38, 051706 (2026)
https://doi.org/10.1063/5.0325392

Physics of Fluids LETTER pubs.aip.org/aip/pof

Defects, corrugation, and temperature govern rarefied-air drag on graphene coatings

Cite as: Phys. Fluids **38**, 051706 (2026); doi: 10.1063/5.0325392
Submitted: 30 January 2026 · Accepted: 6 May 2026 ·
Published Online: 22 May 2026

Samuel Cajahuaringa,[1] Davide Bidoggia,[1] Maria Peressi,[1] and Antimo Marrazzo[2,a)]

AFFILIATIONS

[1]Dipartimento di Fisica, Università di Trieste, I-34151 Trieste, Italy
[2]Scuola Internazionale Superiore di Studi Avanzati (SISSA), I-34136 Trieste, Italy

[a)]Author to whom correspondence should be addressed: amarrazz@sissa.it

ABSTRACT

In rarefied atmospheric environments, where continuum fluid dynamics breaks down, aerodynamic drag is governed by gas–surface momentum exchange, making surface structure and chemistry key design knobs. Using molecular dynamics simulations, we show that coating the α-Al_2O_3(0001) surface with graphene markedly reduces the tangential momentum accommodation coefficient (TMAC) of N_2, shifting scattering toward more specular reflection and thereby lowering drag; we further benchmark this response against graphite. The reduction strengthens up to 900 K. While structural defects can increase TMAC via defect-induced corrugation and local atomic and electronic rearrangements, graphene retains its performance at experimentally relevant defect densities.

The ability to tailor surface drag properties is of profound technological importance, particularly in aerospace applications where vehicles operate in rarefied atmospheric regimes. These environments are characterized by Knudsen numbers exceeding unity, when conventional continuum fluid dynamics fails and gas–surface interactions (GSIs) become the dominant mechanism governing momentum and energy exchange.[1–3] Under such conditions, the drag force is no longer a bulk fluid property but is dictated by atomistic processes at the interface, making surface engineering a critical strategy for enhancing performance, energy efficiency, and thermal management.

Graphene could be a promising coating for rarefied-flow applications because its atomic smoothness, high in-plane stiffness, and relative chemical inertness can promote more specular molecular reflections and reduce tangential momentum transfer to the wall. It is therefore interesting not only as a robust coating but also as a model surface for understanding gas–surface scattering in the noncontinuum regime. Tribological studies support this picture: Graphene exhibits exceptional mechanical strength, chemical stability, and ultralow solid–solid friction, yet these properties are highly sensitive to lattice perfection.[4–9]

In rarefied flows, drag is governed by the tangential momentum accommodation coefficient (TMAC), which measures the efficiency of tangential momentum transfer during molecular collisions with a surface. Lower TMAC values correspond to more specular, slip-like reflections and are therefore favorable for drag reduction, especially for high-altitude and hypersonic platforms.[10] Although graphene is well known for reducing solid–solid friction, its influence on gas–surface drag remains largely unexplored.

A key question is how robust this low-accommodation behavior remains under realistic conditions, where graphene is rarely defect-free. Defects such as Stone–Wales (SW) transformations and vacancies disrupt the hexagonal lattice, generate local strain, and induce out-of-plane corrugation, thereby modifying the interaction landscape sampled by impinging gas molecules. As shown in the defect-engineering literature,[11,12] even sparse defects can strongly alter the interfacial response. This suggests that, just as defects tune graphene's tribological behavior, they may also affect gas–surface momentum accommodation and, ultimately, rarefied-flow drag.

In this work, we investigate how coating alumina with graphene—particularly graphene containing realistic crystalline defects—modifies the drag experienced by nitrogen, the primary constituent of air, in rarefied environments. We compute TMAC and other gas–surface accommodation coefficients as functions of temperature and defect concentration, thereby quantifying how variations in defect density and thermal conditions jointly control rarefied drag while also unraveling the critical role played by defect-driven corrugation.

Aluminum and its alloys are among the most widely used structural materials in aerospace systems.[13,14] However, upon exposure to

ambient air, aluminum rapidly forms a thin native oxide layer composed primarily of amorphous alumina (Al_2O_3).[15–17] This naturally passivating oxide layer, rather than the bare metal, constitutes the true interface with the surrounding gas. Consequently, we consider Al_2O_3 crystals to be a physically realistic proxy for aluminum alloys in studies of air drag under rarefied conditions.

We focus on three different surfaces: graphite, α-Al_2O_3 (0001), and graphene-coated α-Al_2O_3 (see Fig. 1). We use Monte Carlo (MC) sampling of thousands of molecular dynamics (MD) trajectories, which are obtained using the open-source Large-scale Atomic/Molecular Massively Parallel Simulator (LAMMPS)[18] package and HyperQueue[19] (for more details, see the supplementary material).

The graphite surface is modeled as a multilayered slab comprising 1690 carbon atoms arranged in five stacked honeycomb layers (left slab in Fig. 1). The alumina substrate is represented by a stoichiometric Al-terminated α-Al_2O_3 (0001) slab—the thermodynamically most stable termination due to its lowest surface energy among all possible α-Al_2O_3 facets.[20–24] The α-Al_2O_3 slab contains 36 atomic layers, i.e., 12 repetitions of the bulk unit triple-layer motif: Al–O_3–Al (central slab in Fig. 1). Details on the generation and thermalization of the slabs from NPT and NVT MD are discussed in the supplementary material.

For graphene-coated alumina (right slab in Fig. 1), we take into account the inherent lattice mismatch between the hexagonal unit cells of graphene and α-Al_2O_3 (0001). This mismatch induces interfacial strain,[25] which promotes spontaneous wrinkling and corrugation of the graphene layer.[26,27] To mitigate artificial strain and achieve a more physically realistic interface, we identify a common supercell that minimizes the strain on graphene cell by rotating graphene with respect to alumina.[28,29] Details about the interface generation are discussed in Sec. S2 and Fig. S2 of the supplementary material. Nitrogen molecules (N_2) are initially positioned approximately 12 Å above the topmost surface layer of each slab (Fig. 1). This distance exceeds the cutoff radius of the interatomic potential that models the GSI, ensuring that molecules begin their trajectories in free space, initially unaffected by van der Waals (vdW) attraction. This setup allows for a clean initialization of the collision event, consistent with the methodology employed in prior MD studies of gas–surface scattering.[30,31]

Interatomic potentials are selected based on the specific material system: For the graphite slab, the AIREBO[32] potential is used to describe C–C bonding and long-range dispersion interactions. For the α-Al_2O_3 slab, the many-body Vashishta *et al.*[33] potential is employed to accurately capture the complex ionic and covalent interactions within the oxide lattice. As graphene adsorbs only weakly on alumina,[25] the graphene–alumina interaction is modeled by a pairwise Lennard-Jones (LJ) potential parameterized to reproduce the density functional theory (DFT)-derived adsorption curve,[34] computed using QUANTUM ESPRESSO[35–37] with the Perdew–Burke–Ernzerhof (PBE) functional[38] plus Grimme's D3 dispersion correction[39] and using standard solid-state Precision v1.3 pseudopotentials[40–43] (see Sec. S1 of the supplementary material for more details).

As N_2 is the dominant constituent of air (78% by mole fraction), it is a good proxy to study the effect of air drag; the inclusion of oxygen and water is left to future studies. N_2 is modeled as a rigid diatomic molecule and vibrational degrees of freedom are frozen using the SHAKE[44] algorithm to constrain the bond length at its equilibrium value (1.0976 Å). This approximation is well justified for the temperature range considered in this work is below 2000 K and nitrogen molecules remain in the vibrational ground state, while rotational–translational energy exchange dominates the GSI dynamics. The intermolecular potentials governing GSI are selected based on the substrate: For N_2 interacting with graphite or graphene, the LJ potential is employed, as validated in prior molecular beam and MD studies of N_2–carbon systems,[30,45] while for N_2 interacting with α-Al_2O_3 (0001), we use the Morse potential, consistent with recent simulations of N_2–alumina scattering in noncontinuum regimes.[31] A key aspect of this work is the use of two complementary MD protocols targeting distinct physical regimes of gas–surface collisions. The first protocol mimics molecular gas beam experiments, in which a collimated beam of N_2 molecules impinges on the surface at fixed incidence angles and velocities (Fig. 2 and Fig. S3 in the supplementary material).

We perform molecular gas beam scattering simulations for nitrogen molecules impinging on graphite, bare α-Al_2O_3 (0001), and graphene-coated α-Al_2O_3 (0001) surfaces. This enables us to validate our simulation framework, particularly the accuracy of GSI potentials,

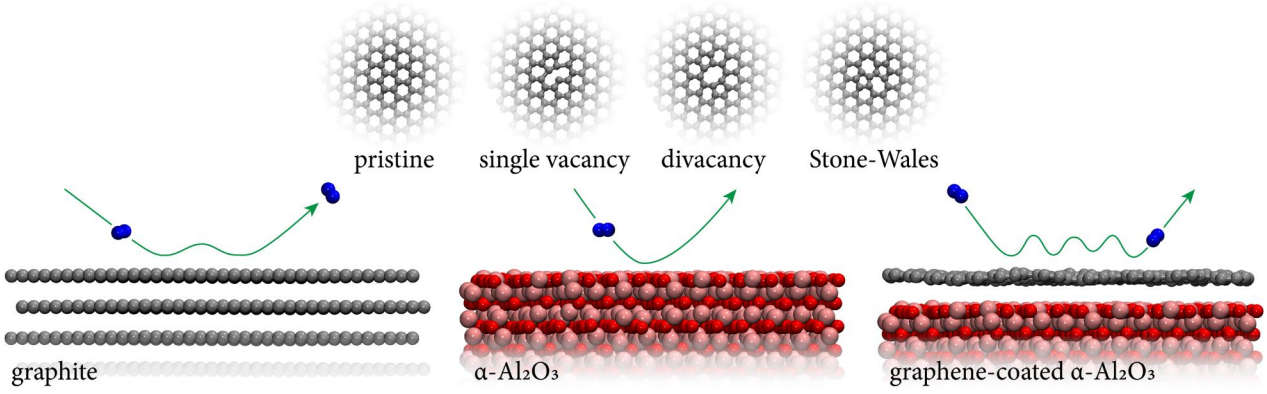

FIG. 1. Schematic representation of the simulated systems. Nitrogen molecule impinging on the multilayer graphite surface, the α-Al_2O_3 (0001) slab, and the graphene-coated α-Al_2O_3 (0001) surface. The inset shows the pristine graphene lattice and the optimized atomic configurations of the key defects studied: single vacancy, divacancy, and Stone–Wales defect.

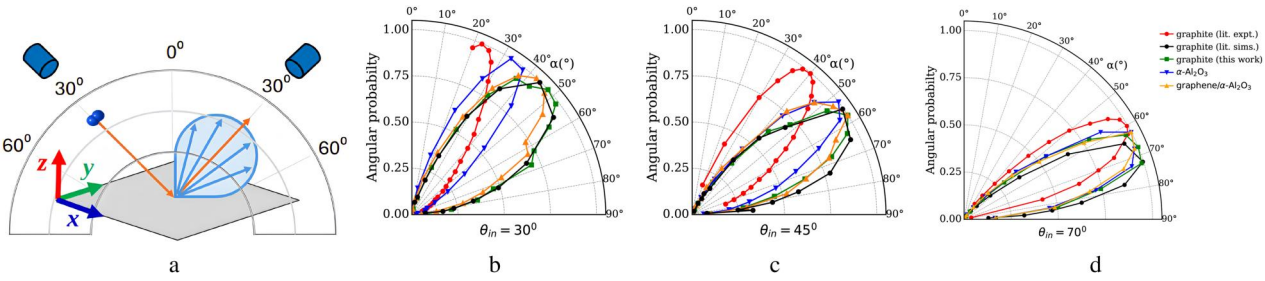

FIG. 2. (a) Schematic representation of gas beam scattering at fixed angle. (b)–(d) Angular distribution of scattered nitrogen molecules on selected surfaces as a function of reflection angle α for three different incidence angles: (b) $\theta_{in} = 30^{\circ}$; (c) $\theta_{in} = 45^{\circ}$; and (d) $\theta_{in} = 70^{\circ}$. Our results for graphite, α-Al_2O_3, and graphene/α-Al_2O_3 are shown by a green line with circles, blue line with squares, and orange line with triangles, respectively. Experimental[30,46] and simulation[30] results on graphite from the literature are represented by red lines with circles and black lines with circles, respectively. A version of these plots in Cartesian coordinates is available in the supplementary material, Fig. S6.

against established experimental and theoretical benchmarks for graphite—a system extensively studied in both beam experiments and MD studies.[30,46,47] While prior studies have reported discrepancies between some numerical predictions and experimental angular distributions for graphite, our primary objective here is not to achieve perfect quantitative agreement with experiment. Instead, we aim to elucidate qualitative behavior and relative trends in scattering across different surface types, with particular emphasis on isolating the respective impacts of structural defects and temperature.

To this end, we replicate the well-characterized experimental setup of Mehta *et al.*:[46] a supersonic N_2 beam with a nominal velocity of 1453 m/s incident at angles of 30°, 45°, and 70° onto a graphite surface held at 677 K under high-vacuum conditions.[30,46,47] The same configuration is applied to alumina-based surfaces to investigate how surface chemistry and graphene coating influence scattering dynamics. For each incidence angle, 4000 independent trajectories are simulated per surface, with a maximum simulation time of 100 ps per trajectory to prevent spurious trapping (for details, see Sec. S5 of the supplementary material). Initial molecular positions, orientations, and velocities are sampled via Monte Carlo importance sampling[48] (for details, see Sec. S2 of the supplementary material), ensuring statistical representativeness and accurate reproduction of beam conditions.

Trajectories are terminated when the scattered molecule reaches a height exceeding the intermolecular cutoff distance above the surface, guaranteeing free-flight conditions for post-collision analysis. The final translational velocities are used to compute angular distributions as a function of the scattering angle α, which reflect the probability of reflection at a given angle. Figures 2(b)–2(d) show the computed angular distributions for pristine alumina, graphene-coated alumina, and graphite at several incidence angles θ_{in}, together with experimental data and simulations from the literature for graphite. Our graphite results agree with prior computational studies[30] and qualitatively reproduce the characteristic scattering profiles reported in experiments.[45,47] As the angular distribution governs the gas–surface momentum exchange, these features directly influence the aerodynamic drag.

At small incidence angles [Figs. 2(b) and 2(c)], the angular distribution for graphene-coated alumina is closer to that of graphite than to that of bare alumina. At the largest incidence angle, $\theta_{\text{in}} = 70^{\circ}$ [Fig. 2(d)], the distributions converge and all three surfaces become nearly indistinguishable.

This behavior can be rationalized as follows. As the angle of incidence increases (at fixed incident speed), the component of the kinetic energy normal to the surface decreases. The incident normal energy therefore becomes small, and energy exchange is dominated by coupling to the thermal motion of the surface atoms. In this regime, particles do not penetrate deeply into the surface potential and primarily sample an effectively averaged, weakly corrugated top layer. For graphite and graphene-coated alumina, this top layer can be viewed as a nearly monatomic, almost flat surface, whereas for alumina it is a slightly corrugated diatomic surface due to the nonperfect coplanarity of Al and O atoms and their different vdW radii, 1.84 and 1.52 Å, respectively. At higher normal incident energies, by contrast, particles can probe and interact with the lateral corrugation of the surface potential, entering the structural scattering regime. Scattering then becomes more sensitive to surface topography and corrugation, and the angular distributions broaden. The relatively low normal energies associated with large incidence angles therefore lead to similar angular distributions for all three surfaces, consistent with previous observations.[47,49]

These results, based on collimated molecular beams with prescribed incidence angle and speed, provide detailed insight into GSI and show that graphene-coated alumina behaves more similarly to graphite than to bare alumina. However, these beam-type simulations are conditional on a narrowly defined initial molecular state. To overcome this limitation, we now move from fixed, collimated beams—chosen previously to enable a direct comparison with molecular beam experiments—to a configuration more relevant for assessing coating performance under realistic flow conditions. In this complementary approach, initial molecular velocities are randomly assigned by sampling from the equilibrium distribution at a given gas temperature. Molecules thus impinge with a distribution of incidence angles and kinetic energies (for details, see Sec. S4 of the supplementary material). The theoretical foundations of this stochastic initialization have been extensively discussed in the literature and will not be repeated here.[30,31,45,47] In many practical situations, the initial molecular state is not fixed as in a molecular beam experiment but reflects a thermalized gas.

Accommodation coefficients (ACs) provide a compact and widely used measure of gas–surface scattering, quantifying the efficiency of momentum and energy transfer during collisions, which could be defined as

$$\alpha_q = \frac{\langle Q_I \rangle - \langle Q_R \rangle}{\langle Q_I \rangle - \langle Q_T \rangle}, \tag{1}$$

where the subscript q denotes a specific kinematic property of the gas molecule, such as its momentum or kinetic energy in a given direction. The brackets denote that the average values for these quantities need to be computed, and the subscripts denote whether the average value is to be computed from the incoming (I) particles, the reflected (R) particles, or the thermal wall distribution (T). The principal limitation of this conventional definition is that it becomes numerically unstable when the gas temperature approaches the surface temperature, i.e., near thermal equilibrium[50] ($\langle Q_I \rangle \approx \langle Q_T \rangle$). This issue is particularly relevant here because our goal is to quantify drag under conditions where the gas and the surface might be in thermal equilibrium.

To overcome this limitation, we adopt the velocity correlation-based method introduced by Spijker *et al.*,[50,51] which remains robust even under isothermal conditions.[50,52–54] In this approach, various ACs are obtained from the slope of a least squares linear fit to the MD collisional data expressed in terms of appropriately defined velocity correlation functions,

$$\alpha_q = 1 - \frac{\sum_i \left(Q_I^i - \langle Q_I \rangle\right)\left(Q_R^i - \langle Q_R \rangle\right)}{\sum_i \left(Q_I^i - \langle Q_I \rangle\right)^2}, \tag{2}$$

where Q_I^i and Q_R^i represent, respectively, the pre-collisional and post-collisional values of the same property for the ith gas particle. We define the TMAC for nitrogen flow along the x direction as

$$TMAC = 1 - \frac{\sum_i \left(p_{I,x}^i - \langle p_{I,x} \rangle\right)\left(p_{R,x}^i - \langle p_{R,x} \rangle\right)}{\sum_i \left(p_{I,x}^i - \langle p_{I,x} \rangle\right)^2}. \tag{3}$$

We calculate TMACs for nitrogen flow at room temperature, with a bulk flow velocity of 280 m/s (representative of a commercial aircraft flight speed), over surfaces also held at room temperature. For each of the three surfaces considered, a total of 10 000 trajectories is simulated to obtain statistically converged TMAC values. The resulting scattering data used to compute the TMACs are summarized in Fig. 3.

Following the approach of Spijker *et al.*,[50] the tangential velocities of molecules crossing a virtual plane before and after collision with the surface are recorded and used to determine the ACs via a linear least squares fit. Figure 3 shows the correlation between incoming and outgoing tangential velocities employed to compute TMAC. The limiting cases where TMAC = 0 and TMAC = 1 are indicated by black dashed lines: The diagonal line corresponds to fully correlated velocities, i.e., purely specular scattering with TMAC = 0, whereas the horizontal line corresponds to completely uncorrelated velocities, i.e., fully accommodated particles with TMAC = 1. The red line represents the best-fit linear regression to the MD data, and its slope is used to obtain the value of TMAC. An increase in the slope corresponds to a decrease in TMAC. For all surfaces, the incoming and outgoing tangential velocities are distributed around the diagonal line and are centered near 280 m/s, corresponding to the imposed flow velocity. For the bare alumina, graphene-coated alumina, and graphite surfaces, we obtain TMAC values of 0.30(1), 0.21(1), and 0.22(1), respectively. The value for alumina is consistent with that reported by Thoudam *et al.*[31] Inspection of the correlation plots reveals that the fraction of specular-like collisions increases for the graphene-coated alumina surface. We observe an approximate 30% reduction in the TMAC of alumina when coated with graphene, approaching that of graphite.

In the rarefied regime, aerodynamic drag is determined by the net momentum flux exchanged between incident and reflected molecules at the surface. Accordingly, a lower TMAC implies more specular-like reflection and reduced tangential momentum transfer to the wall, whereas a higher TMAC promotes more diffuse scattering and larger drag, consistent with classical free-molecular theory and with Maxwell/CLL-based kinetic and DSMC studies showing a strong sensitivity of drag coefficients to the adopted gas–surface interaction model and accommodation parameters.[55–58] From this perspective, the TMAC is a microscopic descriptor of gas–surface scattering, whereas the drag coefficient is a macroscopic aerodynamic quantity resulting from the cumulative effect of many such collisions over the entire body. Therefore, while ACs more directly reflect the intrinsic material-dependent properties of the gas–surface interaction, the drag coefficient also depends on external flow conditions, such as gas composition, velocity, and temperature, as well as on the geometry and orientation of the object.

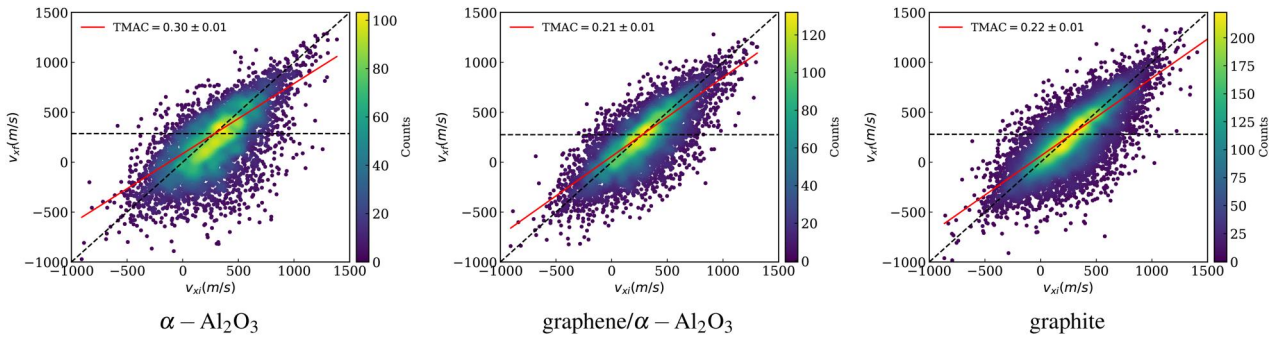

FIG. 3. Correlations between incoming (horizontal axis) v_{xi} and outgoing final v_{xf} (vertical axis) tangential velocity of nitrogen molecules on three different surfaces—alumina, graphene-coated alumina, and graphite—for a gas flow at room temperature with bulk velocity of 280 m/s. The solid red lines demonstrate the least square linear fit of the tangential velocity data to obtain the tangential momentum accommodation coefficients (TMACs).

Studying the temperature dependence of ACs is essential for understanding GSI mechanisms under realistic thermal conditions. In particular, the TMAC directly influences heat and momentum transfer in applications such as thermal protection systems, micro- and nanoscale gas flows, and heterogeneous catalysis. Figure 4 shows the variation of ACs as a function of temperature for two surfaces: bare alumina (blue curves) and graphene-coated alumina (orange curves). For alumina, TMAC exhibits a slight increase up to approximately 500 K, followed by a gradual decrease with further increase in temperature. In contrast, for the graphene-coated alumina surface, TMAC starts from a lower value and displays a more pronounced decay as temperature rises. This behavior indicates that the graphene layer significantly reduces gas–surface momentum exchange and enhances specular reflection, particularly at elevated temperatures. A similar trend has been reported for graphite in a hydrogen environment, where the TMAC decreases with increasing temperature and tends to level off at high temperatures.[59]

We also compute additional ACs to obtain a more comprehensive picture of the GSI dynamics (see Fig. 4). For the energy accommodation coefficient (EAC), which measures the overall energy transfer from the gas to the surface, the bare alumina surface shows little sensitivity to temperature in the range of 0.4–0.445, whereas its graphene-coated counterpart exhibits a clear decrease in EAC with increasing temperature. The normal energy accommodation coefficient (ENAC), quantifying the exchange of kinetic energy in the direction perpendicular to the surface, displays only a weak temperature dependence for both surfaces. The rotational energy accommodation coefficient ($E_{rot}AC$) reveals the most pronounced difference between the two materials. For bare alumina, $E_{rot}AC$ decreases for temperatures above 500 K, mirroring the trend observed for the TMAC. A similar, but more marked, monotonic decrease with temperature is found for the graphene-coated surface. In summary, Fig. 4 demonstrates that graphene coating not only reduces TMAC but this reduction is also present in EAC and $E_{rot}AC$ for increasing temperatures (all correlation graphs for ACs at different temperatures are reported in Figs. S7 and S8 of the supplementary material).

Up to this point, our analysis has focused on the properties of pristine graphene-coated alumina, an idealized scenario. Under realistic conditions, however, graphene is rarely defect-free and typically contains structural imperfections such as vacancies, divacancies, and SW defects.[9,11] These defects can significantly modify the electronic, structural, and interfacial properties of graphene and may therefore influence the underlying GSI mechanisms. Unlike generic rough surfaces, where drag is mainly governed by roughness-induced diffuse scattering, graphene combines exceptional atomic flatness, high mechanical stiffness, and weakly interacting carbon chemistry. These properties can favor more specular reflections and reduced momentum transfer in the pristine case; accordingly, vacancies and divacancies may enhance accommodation not only through local geometric disruption but also through defect-driven ripples[26,60] and possibly chemical interactions.[61–63]

To address this, we investigate how the presence of vacancies, divacancies, and SW defects in graphene coating alumina affects the TMAC. By quantifying the impact of these defects, we aim to gain deeper insight into how realistic surface conditions govern momentum exchange and energy dissipation during gas–surface collisions. Figure 5 shows that defects significantly affect the TMAC of graphene-coated alumina. Following Thiemann *et al.*,[26] we define the defect concentration as the ratio between the number of atoms removed (one/two per vacancy/divacancy) or displaced (two per SW defect) and the total number of atoms in a pristine graphene sheet. Defects are randomly distributed over the graphene layer, subject to the constraint that defect centers are separated by at least six neighbors from each other (inset in Fig. 1). Figure 5 shows the dependence of TMAC on defect density. For each defect density, a single representative configuration is considered; error bars reflect the statistical

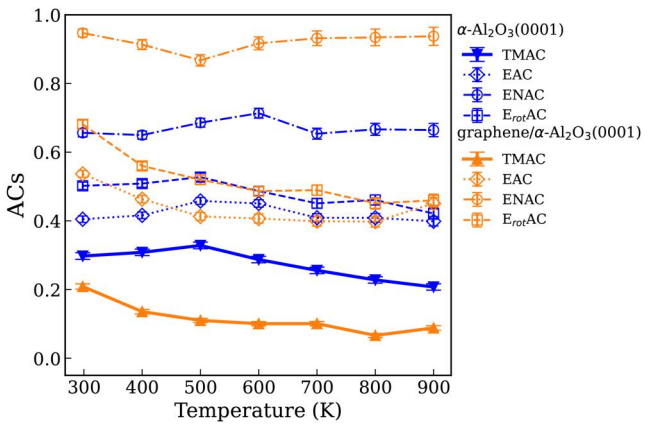

FIG. 4. Temperature dependence of ACs: tangential momentum accommodation coefficient (TMAC), energy accommodation coefficient (EAC), normal energy accommodation coefficient (ENAC), and rotational energy accommodation coefficient ($E_{rot}AC$) for bare alumina (blue lines) and graphene-coated alumina (orange lines). Error bars represent the standard error of the mean computed from the linear regression used to obtain the ACs.

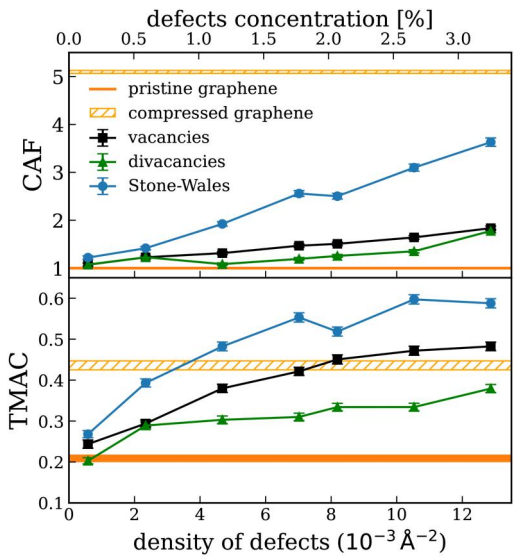

FIG. 5. CAFs (top) and TMACs (bottom) at different density of defects on graphene-coated alumina for vacancies (black squares), divacancies (green triangles), and Stone–Wales defects (light blue circles). The orange and light-orange dashed lines correspond, respectively, to pristine and 2% compressed graphene.

uncertainty associated with the finite sampling of MD collision trajectories and do not include configurational averaging. The results indicate that increasing the density of defects leads to a pronounced increase in TMAC. This trend is mirrored in Fig. 5 where the corrugation amplification factor (CAF) is calculated. Following Thiemann *et al.*,[26] the CAF is defined as the ratio of the height-fluctuation standard deviation of a defective system to that of pristine graphene. As the defect density increases, the CAF rises, indicating that the surface becomes increasingly corrugated or "wrinkled." This enhanced roughness disrupts the specular reflection mechanism characteristic of smooth surfaces and promotes more diffuse scattering events (for more details, see Sec. S7 of the supplementary material), in which tangential momentum is transferred more efficiently to the surface. The correlation between CAF and TMAC suggests that the enhanced surface roughness induced in particular by SW defects is the primary driver of increased tangential momentum transfer. In Sec. S8 of the supplementary material, we report a sensitivity analysis that shows how CAF is robust to variations of the LJ interface well depth by $\pm 10\%$.

To test whether corrugation alone can account for this effect, we simulate pristine graphene under 2% compressive strain—a condition known to induce topographic undulations without introducing atomic-scale defects (for more details, see Sec. S9 of the supplementary material). Remarkably, the TMAC for compressed graphene matches that of vacancy-defective graphene at comparable (but lower) levels of CAF [Fig. 5(a), dashed orange line]. In particular, a TMAC value attained by compressed graphene at CAF $\gtrsim 5.0$ is reproduced in the presence of SW defects at substantially lower corrugation, with CAF < 2. This suggests that, although corrugation appears to be the dominant effect for SW defects, it is unlikely to be the sole mechanism responsible for the associated increase in drag. This is much more evident for vacancies and divacancies, which also lead to significant TMAC enhancement (Fig. 5), yet they produce far less corrugation compared to SW defects at equivalent defect densities (Fig. 5). Despite lower CAF values, vacancies exhibit TMAC increases comparable to those seen in highly corrugated systems.

This decoupling of TMAC from CAF implies that surface roughness is not the dominant mechanism behind TMAC in the case of vacancies and divacancies. Instead, the local lattice distortion around the defects appears to be the critical factor, de-correlating the trajectories of nitrogen molecules and promoting more diffuse scattering. The distinct responses associated with different defect types indicate that multiple physical pathways can enhance TMAC: one mediated by geometric roughness (e.g., SW-driven or strain-induced corrugation) and another driven by topological disruption of the lattice (e.g., vacancies and divacancies).

Experimental studies have shown that the typical vacancy concentration in graphene at room temperature ranges from approximately 10^{-6} to 10^{-4} vacancies/Å^2, depending on the synthesis route and irradiation conditions.[11,12,26] In our simulations, we explore defect concentrations in the range 5.8×10^{-4}–1.287×10^{-2} vacancies/Å^2. Lower, experimentally relevant defect densities were not simulated explicitly because they would require substantially larger surface cells and therefore prohibitively expensive trajectory sampling while also making defect-hit events increasingly rare, so their accommodation coefficients are expected to lie even closer to the pristine-surface limit. Within this range, the lowest TMAC for the vacancy case is 0.24(1), compared with 0.21(1) for pristine graphene-coated alumina, corresponding to a modest increase of about 14%. By contrast, the lowest TMAC for the divacancy case is 0.20(1), effectively identical to that of pristine graphene. These results suggest that, over the range of experimentally relevant defect concentrations, the TMAC is expected to remain essentially unchanged, and a typical density of vacancies in graphene is unlikely to significantly alter gas–surface momentum exchange. Moreover, the trends obtained at higher defect densities may provide useful insight into the behavior of graphene-based coatings under wear or harsh operating conditions, where damage accumulation can generate defect populations well above those expected for as-prepared graphene.

In conclusion, our results demonstrate that coating alumina with a graphene layer effectively reduces the TMAC and, consequently, the drag force at the gas–surface interface. This reduction indicates that the graphene layer promotes more specular gas reflection and limits momentum transfer to the substrate. The effect persists across the entire temperature range considered, with the gap between the TMAC of graphene-coated and bare alumina even increasing with temperature, showing that the low-drag characteristics of graphene are not only maintained but enhanced at high temperatures. A possible extension of the present framework would be to assess nonadiabatic energy-dissipation channels, including electronic excitations during gas–surface collisions, which could be relevant and interesting to explore under more extreme impact conditions. The presence of graphene defects substantially increases drag, an effect partially attributed to defect-induced corrugation. Nevertheless, within the range of experimentally relevant defect concentrations, the TMAC of graphene-coated alumina increases only modestly. Therefore, even under realistic conditions where defects are unavoidable, graphene-coated alumina is expected to retain its ability to significantly reduce the TMAC and thus the drag force at the gas–surface interface.

See the supplementary material for more details on computational protocols and additional results for ACs and CAF.

All authors acknowledge useful discussions with A. Abdurrazaq, D. Acharya, S. de Gironcoli, C. Di Valentin, D. Dragoni, A. Maslov, Z. Muhammad, and C. Scalliet. This work was supported by the ICSC—Centro Nazionale di Ricerca in HPC, Big Data and Quantum Computing, funded by the European Union—NextGenerationEU (CUP Grant. No. J93C22000540006, PNRR Investimento M4.C2.1.4), and Leonardo S.p.A. through the Innovation Grant No. ASGARD. The authors acknowledge CINECA, under CINECA-SISSA, CINECA-UniTS, and ICSC agreements, for providing high-performance computing resources and support. The views and opinions expressed are solely those of the authors and do not necessarily reflect those of the European Union, nor can the European Union be held responsible for them.

AUTHOR DECLARATIONS

Conflict of Interest

The authors have no conflicts to disclose.

Author Contributions

Samuel Cajahuaringa: Data curation (equal); Investigation (equal); Methodology (equal); Resources (equal); Software (equal); Visualization

(equal); Writing – original draft (equal); Writing – review & editing (equal). **Davide Bidoggia:** Data curation (supporting); Investigation (supporting); Methodology (supporting); Visualization (supporting); Writing – original draft (supporting); Writing – review & editing (equal). **Maria Peressi:** Funding acquisition (equal); Investigation (supporting); Methodology (supporting); Project administration (equal); Supervision (equal); Visualization (supporting); Writing – review & editing (equal). **Antimo Marrazzo:** Conceptualization (equal); Funding acquisition (equal); Investigation (equal); Methodology (equal); Project administration (equal); Resources (equal); Supervision (equal); Visualization (equal); Writing – original draft (equal); Writing – review & editing (equal).

DATA AVAILABILITY

The data that support the findings of this study are openly available on the Materials Cloud, Ref. 64.

REFERENCES

[1]G. A. Bird, *Molecular Gas Dynamics and the Direct Simulation of Gas Flows*, reprinted ed., Oxford Engineering Science Series Vol. 42 (Clarendon Press, Oxford, 2003).
[2]I. D. Boyd, *Nonequilibrium Gas Dynamics and Molecular Simulation*, Cambridge Aerospace Series, edited by T. E. Schwartzentruber (Cambridge University Press, Cambridge, 2017).
[3]F. Sharipov, *Rarefied Gas Dynamics* (Wiley-VCH Verlag GmbH & Co. KGaA, Weinheim, 2016).
[4]S. Fan *et al.*, "Structure, superlubricity, applications, and chemical vapor deposition methods of graphene solid lubricants," Tribol. Int. **198**, 109896 (2024).
[5]A. Ayyagari *et al.*, "Progress in superlubricity across different media and material systems-a review," Front. Mech. Eng. **8**, 908497 (2022).
[6]B. Jin *et al.*, "Lubrication properties of graphene under harsh working conditions," Mater. Today Adv. **18**, 100369 (2023).
[7]A. Jafari *et al.*, "Tribological properties of synthetic and biosourced lubricants enhanced by graphene and its derivatives: A review," ACS Omega **9**, 50868 (2024).
[8]A. Zambudio *et al.*, "Fine defect engineering of graphene friction," Carbon **182**, 735 (2021).
[9]F. Banhart *et al.*, "Structural defects in graphene," ACS Nano **5**, 26 (2011).
[10]J. Lee *et al.*, "Statistical assessment of tangential momentum accommodation coefficient using internal flow rate model based on rarefied gas conditions," Results Phys. **43**, 106130 (2022).
[11]M. D. Bhatt *et al.*, "Various defects in graphene: A review," RSC Adv. **12**, 21520 (2022).
[12]S. K. Tiwari *et al.*, "Stone–Wales defect in graphene," Small **19**, 2303340 (2023).
[13]K. Aglawe *et al.*, "Application of aluminum alloys in aviation industry: A review," AIP Conf. Proc. **2804**, 020064 (2023).
[14]S. Li *et al.*, "Development and applications of aluminum alloys for aerospace industry," J. Mater. Res. Technol. **27**, 944 (2023).
[15]N. Cabrera *et al.*, "Theory of the oxidation of metals," Rep. Prog. Phys. **12**, 163 (1949).
[16]J. R. Davis, ed., *ASM Specialty Handbook: Aluminum and Aluminum Alloys* (ASM International, 1993).
[17]J. Evertsson *et al.*, "The thickness of native oxides on aluminum alloys and single crystals," Appl. Surf. Sci. **349**, 826 (2015).
[18]A. P. Thompson *et al.*, "LAMMPS - A flexible simulation tool for particle-based materials modeling at the atomic, meso, and continuum scales," Comput. Phys. Commun. **271**, 108171 (2022).
[19]J. Beránek *et al.*, "HyperQueue: Efficient and ergonomic task graphs on HPC clusters," SoftwareX **27**, 101814 (2024).
[20]J. I. Hütner *et al.*, "Stoichiometric reconstruction of the Al_2O_3 (0001) surface," Science **385**, 1241 (2024).
[21]A. Marmier *et al.*, "*Ab initio* morphology and surface thermodynamics of α-Al_2O_3," Phys. Rev. B **69**, 115409 (2004).
[22]S. Ou *et al.*, "A density functional theory (DFT) investigation of sulfur-based adsorbate interactions on alumina and calcite surfaces," Clays Clay Miner. **70**, 370 (2022).
[23]B. Ramogayana *et al.*, "Density functional theory study of ethylene carbonate adsorption on the (0001) surface of aluminum oxide α-Al_2O_3," ACS Omega **6**, 29577 (2021).
[24]A. Biaggne *et al.*, "Adsorption and surface diffusion of metals on α-Al_2O_3 for advanced manufacturing applications," JOM **73**, 1062 (2021).
[25]D. Acharya *et al.*, "Optimizing the graphene/α-Al_2O_3(0001) interface through minimization of interfacial stress for improved electronic applications," ACS Appl. Nano Mater. **8**, 22626 (2025).
[26]F. L. Thiemann *et al.*, "Defect-dependent corrugation in graphene," Nano Lett. **21**, 8143 (2021).
[27]J.-M. Leyssale *et al.*, "A large-scale molecular dynamics study of the divacancy defect in graphene," J. Phys. Chem. C **118**, 8200 (2014).
[28]P. Lazić, "CellMatch: Combining two unit cells into a common supercell with minimal strain," Comput. Phys. Commun. **197**, 324 (2015).
[29]V. Carnevali *et al.*, "Moiré patterns generated by stacked 2D lattices: A general algorithm to identify primitive coincidence cells," Comput. Mater. Sci. **196**, 110516 (2021).
[30]N. Andric *et al.*, "Molecular dynamics investigation of energy transfer during gas-surface collisions," Phys. Fluids **30**, 077104 (2018).
[31]J. Thoudam *et al.*, "Dynamics of energy transfer between nanoscale aluminum/aluminum oxide particles and nitrogen gas in the noncontinuum regime," J. Phys. Chem. C **128**, 3497 (2024).
[32]S. J. Stuart *et al.*, "A reactive potential for hydrocarbons with intermolecular interactions," J. Chem. Phys. **112**, 6472 (2000).
[33]P. Vashishta *et al.*, "Interaction potentials for alumina and molecular dynamics simulations of amorphous and liquid alumina," J. Appl. Phys. **103**, 083504 (2008).
[34]R. Storn *et al.*, "Differential evolution – A simple and efficient heuristic for global optimization over continuous spaces," J. Global Optim. **11**, 341 (1997).
[35]P. Giannozzi *et al.*, "QUANTUM ESPRESSO: A modular and open-source software project for quantum simulations of materials," J. Phys.: Condens. Matter. **21**, 395502 (2009).
[36]P. Giannozzi *et al.*, "Advanced capabilities for materials modelling with Quantum ESPRESSO," J. Phys.: Condens. Matter **29**, 465901 (2017).
[37]P. Giannozzi *et al.*, "Quantum ESPRESSO toward the exascale," J. Chem. Phys. **152**, 154105 (2020).
[38]J. P. Perdew *et al.*, "Generalized gradient approximation made simple," Phys. Rev. Lett. **77**, 3865 (1996).
[39]S. Grimme *et al.*, "A consistent and accurate *ab initio* parametrization of density functional dispersion correction (DFT-D) for the 94 elements H–Pu," J. Chem. Phys. **132**, 154104 (2010).
[40]G. Prandini *et al.*, "Precision and efficiency in solid-state pseudopotential calculations," npj Comput. Mater. **4**, 72 (2018).
[41]D. Vanderbilt, "Soft self-consistent pseudopotentials in a generalized eigenvalue formalism," Phys. Rev. B **41**, 7892 (1990).
[42]E. Kucukbenli *et al.*, "Projector augmented-wave and all-electron calculations across the periodic table: A comparison of structural and energetic properties," arXiv:1404.3015 [cond-mat.mtrl-sci] (2014).
[43]A. Dal Corso, "Pseudopotentials periodic table: From H to Pu," Comput. Mater. Sci. **95**, 337 (2014).
[44]J.-P. Ryckaert *et al.*, "Numerical integration of the cartesian equations of motion of a system with constraints: Molecular dynamics of n-alkanes," J. Comput. Phys. **23**, 327 (1977).
[45]N. Yamanishi *et al.*, "Multistage gas–surface interaction model for the direct simulation Monte Carlo method," Phys. Fluids **11**, 3540 (1999).
[46]N. A. Mehta *et al.*, "Nonreactive scattering of N_2 from layered graphene using molecular beam experiments and molecular dynamics," J. Phys. Chem. C **122**, 9859 (2018).
[47]N. A. Mehta and D. A. Levin, "Molecular-dynamics-derived gas–surface models for use in direct-simulation Monte Carlo," J. Thermophys. Heat Transfer **31**, 757 (2017).
[48]S. Cajahuaringa *et al.*, "MassCCS: A high-performance collision cross-section software for large macromolecular assemblies," J. Chem. Inf. Model. **63**, 3557 (2023).

[49]C. T. Rettner *et al.*, "Angular and velocity distributions characteristic of the transition between the thermal and structure regimes of gas-surface scattering," Phys. Rev. Lett. **67**, 2183 (1991).
[50]P. Spijker *et al.*, "Computation of accommodation coefficients and the use of velocity correlation profiles in molecular dynamics simulations," Phys. Rev. E **81**, 011203 (2010).
[51]P. Spijker *et al.*, "Velocity correlations and accommodation coefficients for gas-wall interactions in nanochannels," AIP Conf. Proc. **1084**, 659–664 (2008).
[52]D. Bayer-Buhr *et al.*, "Determination of thermal accommodation coefficients on $CaSiO_3$ and SiO_2 using molecular dynamics and experiments," Int. J. Heat Mass Transfer **183**, 122219 (2022).
[53]S. Mohammad Nejad *et al.*, "The influence of gas–wall and gas–gas interactions on the accommodation coefficients for rarefied gases: A molecular dynamics study," Micromachines **11**, 319 (2020).
[54]S. Mohammad Nejad *et al.*, "Modeling rarefied gas-solid surface interactions for Couette flow with different wall temperatures using an unsupervised machine learning technique," Phys. Rev. E **104**, 015309 (2021).
[55]L. H. Sentman, "Free molecule flow theory and its application to the determination of aerodynamic forces," Technical Report No. LMSC-448514 (Lockheed Missiles and Space Company, 1961).
[56]R. G. Lord, "Direct simulation Monte Carlo calculations of rarefied flows with incomplete surface accommodation," J. Fluid Mech. **239**, 449 (1992).
[57]A. Walker *et al.*, "Drag coefficient model using the Cercignani–Lampis–Lord gas–surface interaction model," J. Spacecr. Rockets **51**, 1544 (2014).
[58]D. Kalempa *et al.*, "Drag and thermophoresis on a sphere in a rarefied gas based on the Cercignani–Lampis model of gas-surface interaction," J. Fluid Mech. **900**, A37 (2020).
[59]V. L. Kovalev *et al.*, "Accommodation coefficients for molecular hydrogen on a graphite surface," Fluid Dyn. **45**, 975 (2010).
[60]F. L. Thiemann *et al.*, "Defects induce phase transition from dynamic to static rippling in graphene," Proc. Natl. Acad. Sci. U. S. A. **122**, e2416932122 (2025).
[61]G. Carraro *et al.*, "Influence of defects and heteroatoms on the chemical properties of supported graphene layers," Coatings **12**, 397 (2022).
[62]A. Z. Jovanović *et al.*, "Reactivity of Stone–Wales defect in graphene lattice – DFT study," FlatChem **42**, 100573 (2023).
[63]J. Kumar *et al.*, "Stone–Wales defect and vacancy-assisted enhanced atomic orbital interactions between graphene and ambient gases: A first-principles insight," ACS Omega **5**, 31281 (2020).
[64]S. Cajahuaringa *et al.* (2026). "Defects, corrugation and temperature govern rarefied-air drag on graphene coatings," Materials Cloud Archive, 2026.88. https://doi.org/10.24435/materialscloud:2h-f5

Supplementary Material

Defects, Corrugation and Temperature Govern Rarefied-Air Drag on Graphene Coatings

Samuel Cajahuaringa,[1] Davide Bidoggia,[1] Maria Peressi,[1] and Antimo Marrazzo[2]
[1)] *Dipartimento di Fisica, Università di Trieste, I-34151 Trieste, Italy*
[2)] *Scuola Internazionale Superiore di Studi Avanzati (SISSA), I-34136 Trieste, Italy*

(Dated: 23 April 2026)

CONTENTS

S1. GRAPHENE-ALUMINA INTERFACE

Computational Setup and Interface Construction

All first-principles calculations are performed using the QUANTUM ESPRESSO distribution[1–3] and SSSP Precision v1.3 pseudopotentials[4–7]. First-principles structural optimizations are performed to establish reference geometries for the isolated components. Pristine graphene is optimized using the Perdew-Burke-Ernzerhof (PBE) functional[8] augmented with Grimme's D3 dispersion correction[9] (PBE+D3). A plane-wave kinetic energy cutoff of 50 Ry is applied to the wavefunctions, with a corresponding charge density cutoff of 450 Ry, and Brillouin zone integration employed a $12 \times 12 \times 1$ Monkhorst-Pack k-point grid. These calculations yield an optimized graphene lattice parameter of $a = 2.466$ Å. Bulk α-$Al_2O_3(0001)$ is optimized at the PBE level using again a plane-wave kinetic energy cutoff of 50 Ry for wavefunctions, with a charge density cutoff of 450 Ry and $12 \times 12 \times 5$ Monkhorst-Pack k-point grid, resulting in lattice constants of $a = 4.81$ Å and $c = 13.1454$ Å.

The α-$Al_2O_3(0001)$ slab is made of four layers, where the top and bottom aluminum layers are fully relaxed to obtain a surface structure consistent with established literature[10–15]. Calculations are performed with the PBE+D3 functional, a wavefunction cutoff of 50 Ry, a charge density cutoff of 450 Ry, and $12 \times 12 \times 5$ Monkhorst-Pack k-point grid.

To construct a commensurate graphene/α-$Al_2O_3(0001)$ interface while minimizing lattice mismatch, the graphene sheet is rotated by 26 degrees relative to the substrate. This rotation reduces the lattice mismatch to a negligible 0.04% of strain, enabling the construction of a common supercell matching the surface area of a (4×4) α-$Al_2O_3(0001)$ slab, resulting in a system of 422 atoms for the interface.

DFT absorption calculations

Interfacial binding properties are evaluated using the PBE+D3 functional with a plane-wave kinetic energy cutoff of 50 Ry for the wavefunction and 450 Ry for the charge density, a $3 \times 3 \times 1$ Monkhorst-Pack k-point grid and a vacuum buffer of 20 Å. The computed binding energy and equilibrium separation distance are in agreement with the values reported by D. Acharya et al.[12].

	$\Delta E_{abs}(eV/C)$	d_{abs} (Å)
This work	-0.050	3.08
Debito et al.[12]	-0.051	2.67-3.16

TABLE S1. $\Delta E_{abs}(eV/C)$ is the adsorption energy per carbon atom and d_{abs} is the adsorption distance between graphene and alumina surface.

Alt text: Table comparing adsorption energy per carbon atom and adsorption distance for graphene on alumina, as obtained in this work and by Debito et al.. The adsorption energy is approximately -0.05 eV per carbon atom in both cases. The adsorption distance is 3.08 Åin this work and ranges from 2.67 to 3.16 Åin the reference, showing good agreement between the results.

The relatively low magnitude of the adsorption, characteristic of physisorption, combined with the absence of significant charge transfer across the interface, confirms that the graphene–alumina interaction is predominantly governed by van der Waals forces.

Classical Force Field Parameterization

Given the non-covalent nature of the interface, a Lennard-Jones (LJ) pair potential is developed to describe the Al–C and O–C interactions. The LJ parameters are optimized by fitting the DFT adsorption energy curve using the differential evolution optimization method[16]. The population consists of 40 individuals and the space region is limited by 0.005—0.04 eV for ε_{Al-C}, 2.9—3.5 Å for σ_{Al-C}, 0.002—0.005 eV for ε_{O-C} and 2.0—3.1 Å for σ_{O-C}, with mutation factor 0.5 and cross rate 0.8. We use a custom cost function defined by a weighted mean absolute error (WMAE) between the LAMMPS-computed binding energies and the reference DFT energies across the interfacial separation profile:

$$WMAE = \frac{\sum_i w_i |E_i^{LJ} - E_i^{DFT}|}{\sum_i w_i} \tag{S1}$$

where the weighting factor is defined as $w_i = 1/(|E_i^{DFT} - E_{min}^{DFT}| + \delta)$, with $\delta = 10^{-6}$ eV introduced for numerical stability. This inverse-energy weighting scheme deliberately amplifies the contribution of data points near the potential energy minimum,

	$\varepsilon(eV)$	σ (Å)
Al-C	0.0112	3.242
O-C	0.0049	2.073

TABLE S2. LJ parameters optimized with DFT (PBE+D3) for graphene on α-$Al_2O_3(0001)$.

Alt text: The optimized Lennard-Jones parameters for the Al-C interaction are $\varepsilon = 0.0112$ eV and $\sigma = 3.242$ Å, while for the O-C interaction, $\varepsilon = 0.0049$ eV and $\sigma = 2.073$ Å.

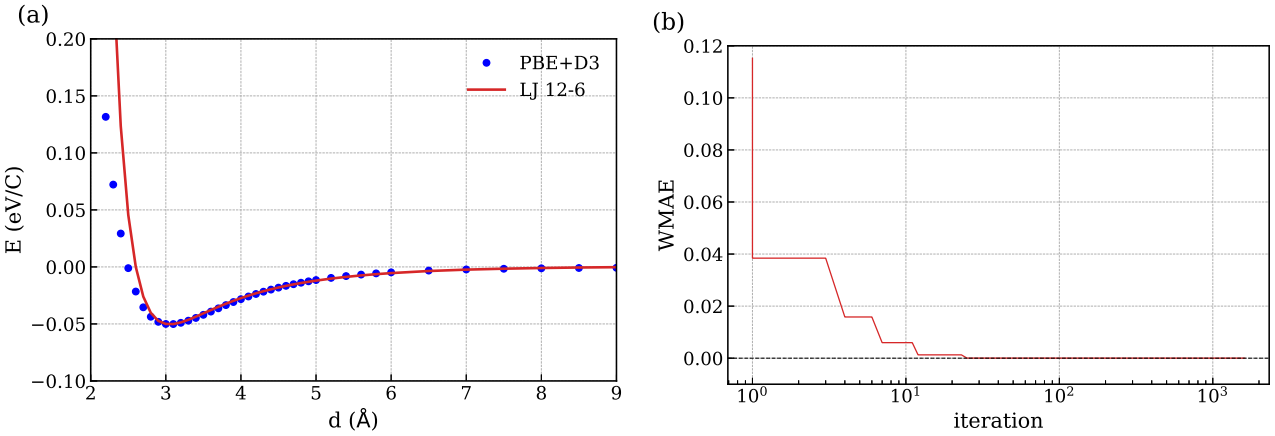

FIG. S1. (a) Adsorption energy profile computed with DFT and the corresponding optimized LJ force field. (b) WMAE evolution of best individual as function of numbers of iterations.

Alt text: Panel (a) shows the adsorption energy profile for graphene on alumina as a function of interfacial separation, comparing DFT results with the optimized Lennard-Jones potential. The two curves show good agreement, particularly near the energy minimum correctly reproducing the equilibrium binding distance and well depth. Panel (b) illustrates the convergence of the optimization process, with the weighted mean absolute error monotonicallydecreasing over iterations.

ensuring that the equilibrium binding distance and well depth are reproduced with high fidelity (see Fig. S1a). The optimized LJ parameters are reported in the Table S1.

The resulting fitted potential demonstrates well agreement with the reference DFT data. This validates the transferability of the derived force field for subsequent large-scale molecular dynamics simulations of graphene/α-alumina systems.

S2. COMPUTATIONAL DETAILS

Generation and thermalization of slabs.

To generate these slabs, we first compute the equilibrium lattice constants for the bulk crystals (with hexagonal symmetry) under an isothermal-isobaric (NPT) ensemble from room temperature until 900 K and 1 atm pressure for 100 ps to compute the thermal averages. Periodic boundary conditions are applied in all three spatial dimensions during the bulk equilibration phase. To build the graphene-coated α-$Al_2O_3(0001)$ structures, we follow the protocol displayed in Fig. S2. We select the alumina and graphene units cell relaxed at a given temperature (T_0), then for each temperature we build a common supercell (not necessarily hexagonal) which accomodates both alumina and graphene allowing for a small strain in the latter using the CellMatch code[17]. We try different relative orientation between the cells until a common supercell with a strain for graphene less than 0.0001 (area ratio) is obtained. Calculations for bare alumina α-$Al_2O_3(0001)$ surface are performed on the same structures by removing carbon atoms.

Before thermalization, the atomic coordinates of each surface are optimized via energy minimization to eliminate any residual strain or unphysical forces. Following minimization, the surfaces are equilibrated in the canonical (NVT) ensemble for 100 ps to ensure thermal stability before introducing gas molecules.

We use the graphene-coated α-$Al_2O_3(0001)$ surface structure at room temperature to create the interfaces with different concentration of defects; except for the lowest concentration of defects (0.14%), where we considered a $2 \times 2 \times 1$ supercell.

T (K)	$a_{Al_2O_3}$ (Å)	a_{Gr} (Å)
298	4.7912	2.4168
400	4.7997	2.4164
500	4.8082	2.4162
600	4.8171	2.4161
677	4.8237	2.4161
700	4.8258	2.4161
800	4.8353	2.4161
900	4.8447	2.4162

TABLE S3. Lattice parameters for alumina and graphene as a function of temperature, modeled by Vashishta[18] and AIREBO[19] potentials, respectively.

Alt text: Table listing the lattice parameters for alumina and graphene at various temperatures. The lattice parameter for alumina increases from 4.7912 Å at 298 K to 4.8447 Å at 900 K, while the lattice parameter for graphene remains nearly constant around 2.416 Å across the temperature range.

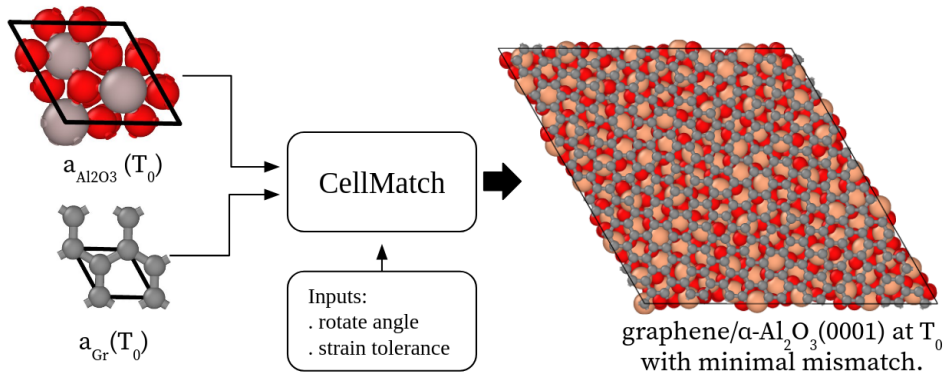

FIG. S2. Workflow to build the relaxed graphene-coated alumina surface at different temperatures.

Alt text: Schematic workflow for constructing the relaxed graphene-coated alumina surface. The process consistes in the optimiztion of both alumina and graphene structures at a given temperature, then the construction of a common supercell with minimal strain utilizing the CellMatch code.

Task farming

The large-scale computation of scattering trajectories constitutes a heterogeneous workload because trajectories are sampled over a wide range of initial conditions, leading to variable run times across tasks. This type of *embarrassingly parallel* workload is commonly referred to as *task farming*. We therefore employ HyperQueue[20], a meta-scheduler for task farming that operates on top of high-performance computing (HPC) workload managers. HyperQueue groups many fine-grained tasks into a smaller number of scheduler allocations and then dynamically load-balances tasks across allocated nodes and cores.

S3. MONTE CARLO SAMPLING OF MOLECULAR-BEAM SCATTERING

In order to mimic traditional molecular gas beam experiments, where a collimated beam of N_2 molecules is directed toward the surface at fixed incidence angles and velocities, each trajectory is initialized with a prescribed speed (sampled from a narrow distribution centered on the experimental beam velocity) and a defined incident polar angle θ_i, while the lateral position and azimuthal orientation are randomized over the surface. Fig. S3a illustrates the scattering trajectory of a nitrogen molecule on a graphite surface. The initial conditions of a linear molecule such as N_2 are specified by the following variables:

$$\mathbf{r}_i = (x_i, y_i, r_c; \theta_r, \phi_r), \tag{S2}$$

$$\mathbf{v}_i = (-v\sin\theta_i\cos\phi, -v\sin\theta_i\sin\phi, -v\cos\theta_i) \tag{S3}$$

$$\omega_i = (\omega, \psi) \tag{S4}$$

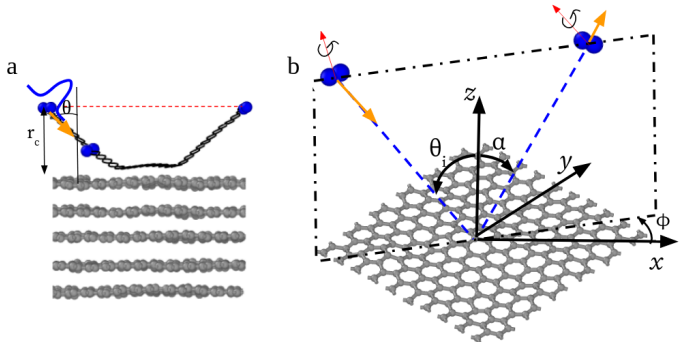

FIG. S3. Gas beam scattering at fixed incoming angle: (a) example of scattering trajectory, (b) Incident and reflected velocities.

Alt text: Panel (a) illustrates a scattering trajectory of a nitrogen molecule on a graphite surface. θ angle is here defined as the incident angle. Panel (b) shows the incident and reflected velocity vectors, defining α as the reflected angle and ϕ as the azimuthal angle. Conventionally the z axis is taken to be normal to the surface.

where $\mathbf{r}_i$ describes the position of the center of the molecule, while θ_r and ϕ_r represent its orientation. $\mathbf{v}_i$ is the velocity of center and ω_i its angular velocity. The gas molecules are launched from a fixed height above the surface, $z = r_c$. Their lateral position and molecular orientation are randomized across the surface, and can be sampled as

$$x_i = L_x \xi_1, \tag{S5}$$
$$y_i = L_y \xi_2, \tag{S6}$$
$$\phi_r = 2\pi\xi_3, \tag{S7}$$
$$\theta_r = \sin^{-1}(2\xi_4 - 1) + \frac{\pi}{2}. \tag{S8}$$

where L_x and L_y are determined by the lateral dimensions of the surface, and $\xi_1, \xi_2, \xi_3, \xi_4$ are random variables uniformly distributed on the interval $[0,1]$. The incident (translational and rotational) velocities are set at a fixed incidence angle θ_i, with a random azimuthal orientation given by $\phi = 2\pi\xi_5$.

Gas beam scattering experiments on graphite were carried out under the following conditions: a supersonic N_2 beam was formed by expanding the gas through a pinhole nozzle of 125 μm diameter. The nozzle was held at 296 K, yielding N_2 molecules with a nominal velocity of $v = 1453$ m/s and a velocity width (full width at half maximum, FWHM) of $\Delta v = 151$ m/s[21].

A supersonic molecular beam is not simply a thermal gas at equilibrium (as described by the Maxwell-Boltzmann distribution), but rather a beam produced by the expansion of a gas through a nozzle. When a gas expands from high pressure through a nozzle into vacuum, a substantial fraction of its random thermal energy is converted into directed (streaming) motion along the beam axis. The molecules are accelerated because the high-pressure gas upstream of the nozzle drives the flow, while collisions within the expansion region redistribute thermal motion into coherent bulk velocity. This process can be approximated as an adiabatic expansion, leading to a terminal beam speed of

$$v \approx \sqrt{\frac{2\gamma}{\gamma - 1}\frac{k_B T_0}{m}} = 1450 \quad m/s \tag{S9}$$

where $T_0 = 296$ K is the nozzle temperature, $m = 14.007$ amu is the N_2 mass and γ the adiabatic coefficient, that is equal to 7/5 for diatomic molecules. In a nozzle expansion, most translational thermal motion is converted into directed flow, but rotational degrees of freedom still in thermal equilibrium and described by the Maxwell-Boltzmann distribution. The velocities (translational and rotational) are sampled by:

$$v \Leftarrow \mathcal{N}(v, \sigma = \Delta v/(8\ln 2)) \tag{S10}$$
$$\phi = 2\pi\xi_6 \tag{S11}$$
$$\omega \Leftarrow \frac{I}{K_B T_0}\omega e^{-\frac{I\omega^2}{2K_B T_0}} \tag{S12}$$

where I is the moment of inertia of the molecule, ω is the magnitude of its angular velocity, and ψ denotes the ratio of the angular-velocity components in the molecular frame[22].

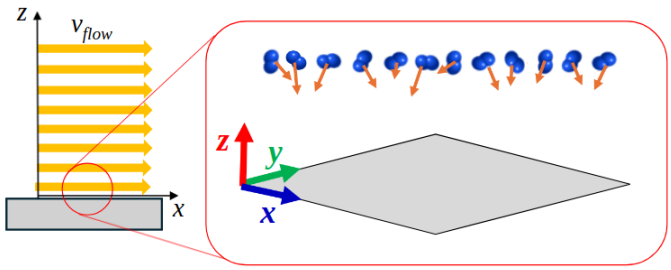

FIG. S4. Schematic representation of a rarefied gas flow interacting with a surface; at the microscopic level, the gas is assumed to be in thermal equilibrium with a drift velocity tangential to the surface.

Alt text: The gas flow is oriented along the x axis direction, parallel to the surface, while the thermal velocity distribution of the gas molecules is represented by a Maxwell-Boltzmann distribution centered around this non-zero drift velocity.

S4. MONTE CARLO SAMPLING OF RAREFIED GAS-FLOW SCATTERING

In order to study drag induced by a gas flow (Fig. S4) under highly rarefied conditions, it is necessary to sample the full range of molecular initial velocities, rather than restricting the dynamics to a fixed incidence angle and a narrowly distributed beam speed. This can be achieved by drawing translational and rotational velocities from the equilibrium distributions at a prescribed temperature. The numerical setup is otherwise analogous to that described in the previous section. The initial molecular position and orientation are sampled using Eq. (S2); in the present case, the translational and rotational velocities are drawn from the corresponding Maxwell-Boltzmann distributions, given by

$$v_x \Leftarrow \sqrt{\frac{m}{2\pi K_B T}} e^{-\frac{m}{2K_B T}(v_x - v_{flow})^2}, \tag{S13}$$

$$v_y \Leftarrow \sqrt{\frac{m}{2\pi K_B T}} e^{-\frac{m}{2K_B T} v_y^2}, \tag{S14}$$

$$v_z \Leftarrow \frac{m}{K_B T} v_z e^{-\frac{m}{2K_B T} v_z^2} \quad v_z < 0, \tag{S15}$$

$$\phi = 2\pi\xi_7 \tag{S16}$$

$$\omega \Leftarrow \frac{I}{K_B T_0} \omega e^{-\frac{I\omega^2}{2K_B T_0}}, \tag{S17}$$

In this case, v_x denotes the molecular velocity component along the flow direction, v_y is the tangential component perpendicular to the flow, and v_z is the normal component, which by convention is taken to be positive when pointing away from the surface. The rotational velocities are described following the same convention as in the previous section.

S5. COLLISION STATISTICS FOR SCATTERING TRAJECTORIES

Fig. S5 summarizes the collision statistics for the three surfaces considered: graphite, α-$Al_2O_3(0001)$, and graphene-coated α-$Al_2O_3(0001)$. Bars shown in bold colors correspond to single-collision events, whereas lighter shades indicate trajectories undergoing multiple collisions before escaping from the surface. In our gas-beam simulations, all molecules are ultimately reflected and we do not observe nitrogen trapping on any surface. This is ensured by employing a sufficiently long maximum simulation time (100 ps), which minimises the risk of misclassifying slowly desorbing trajectories and thereby improves the accuracy of the extracted angular distributions.

Fig. S6 is the angular scattering distribution for the three surfaces considered in this study.

S6. ACCOMMODATION COEFFICIENTS

To compute the accommodation coefficients (ACs), we first collect collision data from the MD simulations and then analyse the correlations between the relevant incoming and outgoing velocity components[23]. These correlations can be represented as two-dimensional probability-density maps: for a given set of incident translational and rotational velocities, they provide the

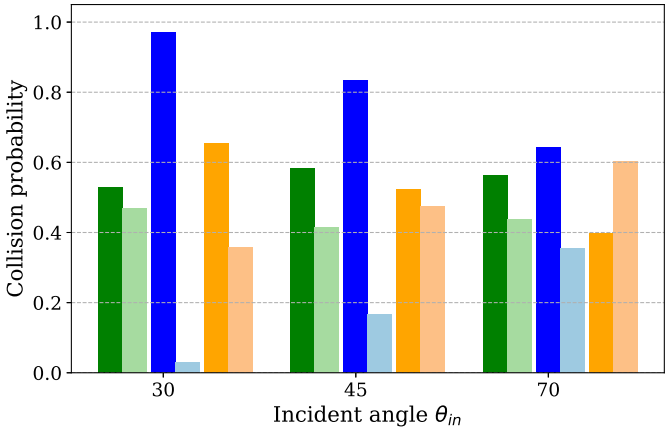

FIG. S5. Collision statistics for N_2 scattering-trajectory simulations on (i) a multilayer graphite surface (green shades), (ii) an α-$Al_2O_3(0001)$ slab (blue shades), and (iii) a graphene-coated α-$Al_2O_3(0001)$ slab (orange shades). Bold colours indicate single-collision events, whereas lighter shades denote multiple-collision trajectories that ultimately escape from the surface.

Alt text: Bar chart showing the collision statistics for nitrogen scattering trajectories on three different surfaces: graphite, alumina, and graphene-coated alumina at different impingement angles (30, 45, and 70 degrees). For each surface, the bars are divided into two categories: single-collision events and multiple-collision events. The chart indicates that for all three surfaces and all impingement angles, the majority of trajectories are single-collision events. An exception is the case of graphene-coated alumina at 70 degrees, where multiple-collision events are more prevalent.

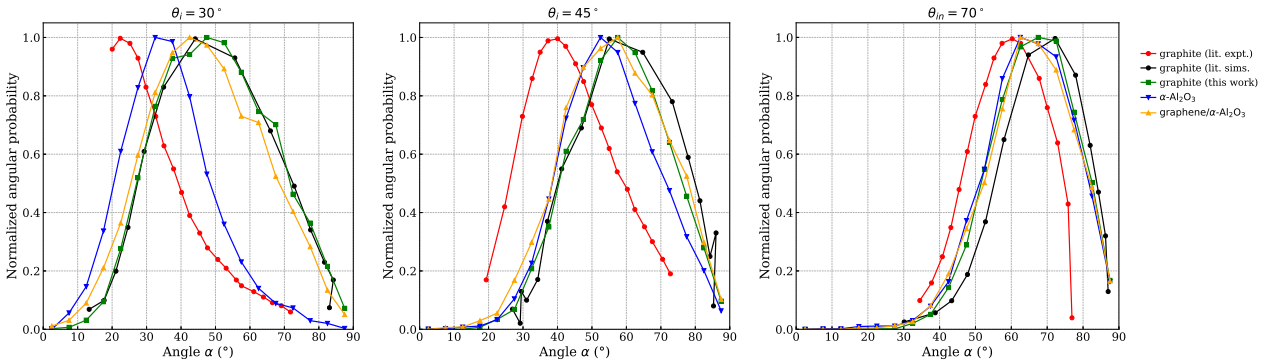

FIG. S6. Cartesian plot version of Fig. 2 in the main text.

Alt text: Angular distribution of reflected trajectories for nitrogen scattering on three different surfaces: graphite, alumina, and graphene-coated alumina at different impingement angles (30, 45, and 70 degrees) compared with teoretical and experimental data from litterature. It represents a Cartesian plot of the polar plot shown in Fig. 2 in the main text.

corresponding distribution of reflected velocities (see Figs. S7 and S8). We then fit a straight line to the collision data using a least-squares procedure (red line). The slope of this fit corresponds to the fractional term in Eq. (2) of the main text; by comparing it with the horizontal dashed line (fully diffusive limit) and the diagonal dashed line (fully specular limit), we extract the accommodation coefficient.

S7. PROPORTION OF SPECULAR VS. DIFFUSIVE SCATTERING

Fig. S9 reports the fraction of reflected trajectories as a function of defects concentration in graphene coated alumina for vacancies, divacancies, and Stone-Wales defects in the TAC calculations. Unlike the gas-beam simulations—where the incident angle and kinetic energy are fixed—the TAC framework samples molecules impinging with a broad range of orientations and energies. Consequently, a finite fraction of low-energy molecules becomes trapped at the surface, which is unavoidable even when using long maximum propagation times (100 ps).

For pristine graphene, as well as for vacancy, divacancy and Stone-Wales defects, we observe comparable reflected fractions,

indicating that surface corrugation is not the dominant factor underlying the TAC increase in these cases.

S8. CORRUGATION SENSITIVE ANALYSIS

Figure S10 shows the CAF as function of defect concentration for; vacancies, divacancies and Stone-Wales varying the interface well depth of alumina-graphene interactions by $\pm 10\%$. We note that CAF is virtually unchanged, due the week absorption of graphene on alumina surface, in agreement with Ref.[12].

S9. STRAINED GRAPHENE ON ALUMINA AND CORRUGATION

Different lattice parameters are chosen to impose controlled strain on pristine graphene supported on the alumina surface. Figure S11 shows the corrugation amplification factor (CAF) for strained pristine graphene on alumina. As expected, the CAF increases with increasing compressive strain[24]. In particular, pristine graphene under 2% compressive strain exhibits a CAF of 5.1, which is larger than the maximum value obtained for the defective graphene cases (Stone–Wales), for which CAF = 3.63.

We therefore select pristine graphene at 2% compressive strain for the TAC calculations reported in Fig. 5b of the main text. Since this system contains no lattice defects, the results indicate that corrugation is a primary driver of the TAC enhancement. A similar effect can also be induced by defects, although to different extents: this is evident for vacancy and divacancy defects, which produce a comparatively smaller increase in corrugation.

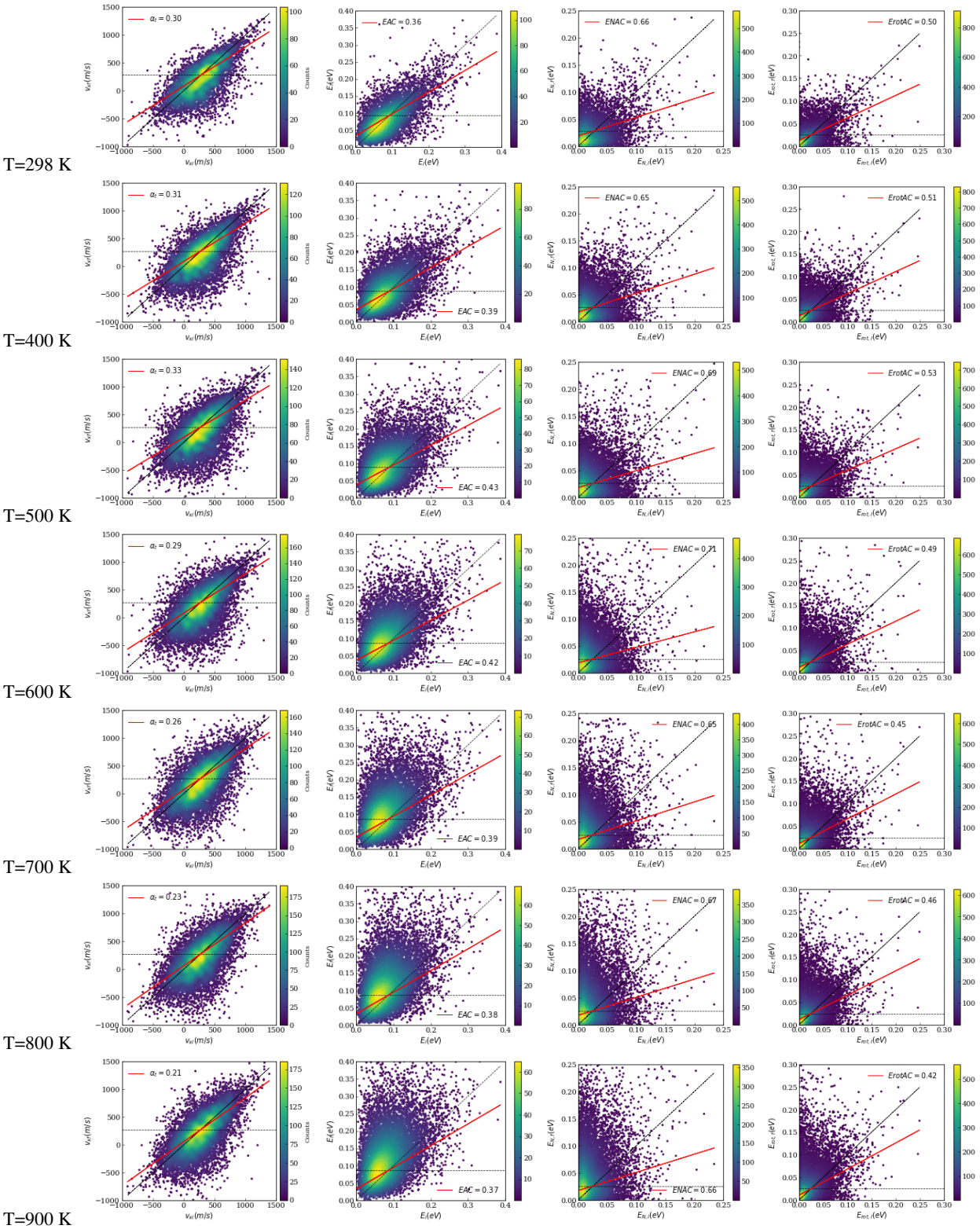

FIG. S7. TMAC, EAC, ENAC, and E_{rot}AC are obtained from the correlation between incident and reflected quantities for the alumina surface. The dashed horizontal and diagonal lines indicate the fully diffusive and fully specular limits, respectively. The red line denotes the least-squares linear fit to the collision data extracted from the MD simulations.

Alt text: The figure presents scatter plots with the fit for the accommodation coefficients (TMAC, EAC, ENAC, and E_{rot}AC) for the alumina surface as a function of temperature.

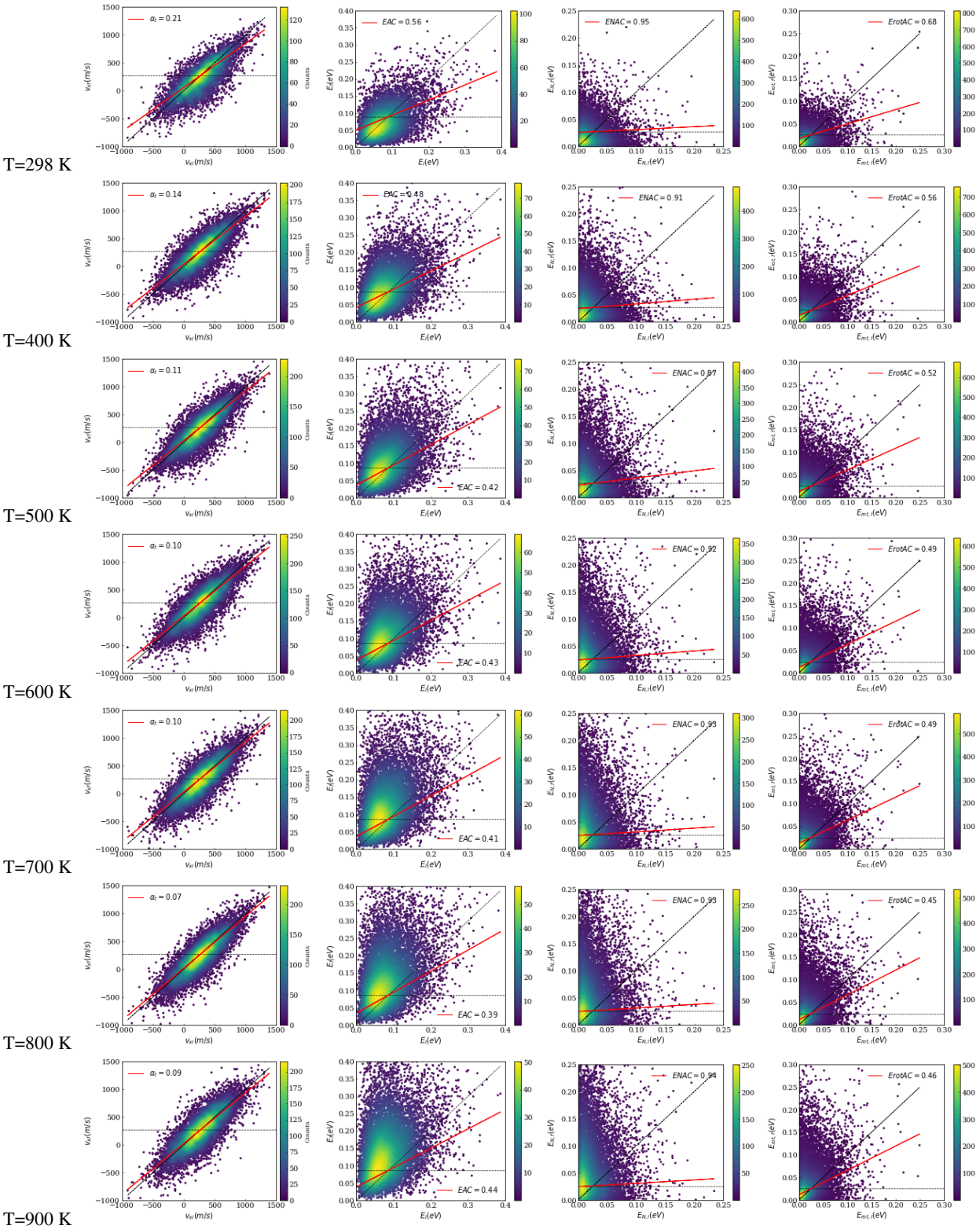

FIG. S8. TMAC, EAC, ENAC, and E_{rot}AC are obtained from the correlation between incident and reflected quantities for graphene-coated alumina. The dashed horizontal and diagonal lines indicate the fully diffusive and fully specular limits, respectively. The red line denotes the least-squares linear fit to the collision data extracted from the MD simulations.

Alt text: The figure presents scatter plots with the fit for the accommodation coefficients (TMAC, EAC, ENAC, and E_{rot}AC) for the graphene-coated alumina surface as a function of temperature.

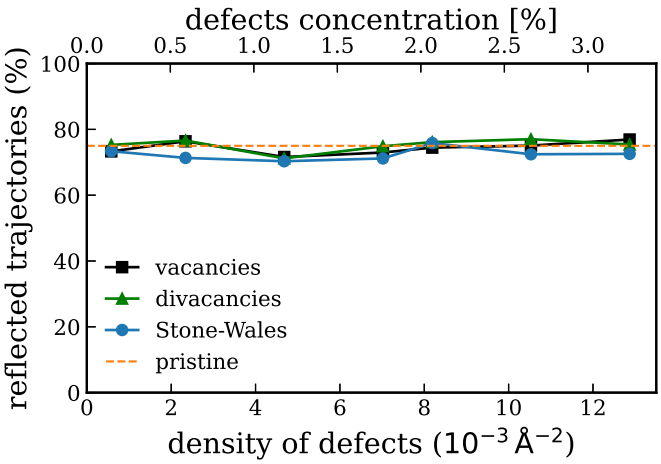

FIG. S9. Percentage of reflected trajectories as a function of defects concentration for vacancies (black circles), divacancies (green squares), and Stone-Wales defects (light-blue circles) in graphene. The orange dashed line indicates the pristine graphene reference.

Alt text: The plot shows the percentage of reflected trajectories as a function of defect concentration for pristine graphene and the three types of defects (vacancies, divacancies, and Stone-Wales) as a function of defect concentration. The percentage, close to 75% for all the cases, remains relatively constant across the range of defect concentrations.

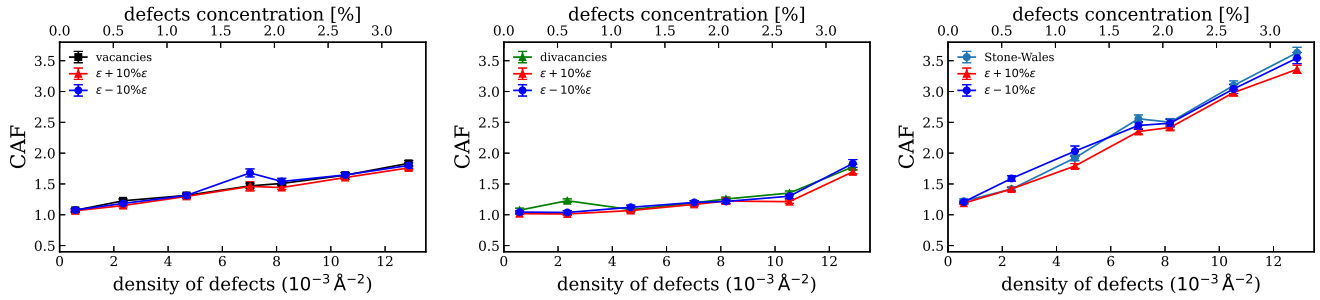

FIG. S10. Sensitivity analysis for CAF vs. defect concentration in the case of vacancies (left), divacancies (center) and Stone-Wales (right). The red and blue lines correspond to results obtained with a modified LJ potential where the well energy ε is respectively increased or decresed by 10%.

Alt text: The three panels show the corrugation amplification factor (CAF) as a function of defect concentration for vacancies, divacancies, and Stone -Wales defects, respectively. In each panel together with the curve obtained with the fitted LJ potential we also report the results obtained by modifying the LJ potential well depth ε by $\pm 10\%$. The results show that the CAF is almost insensitive to these modifications.

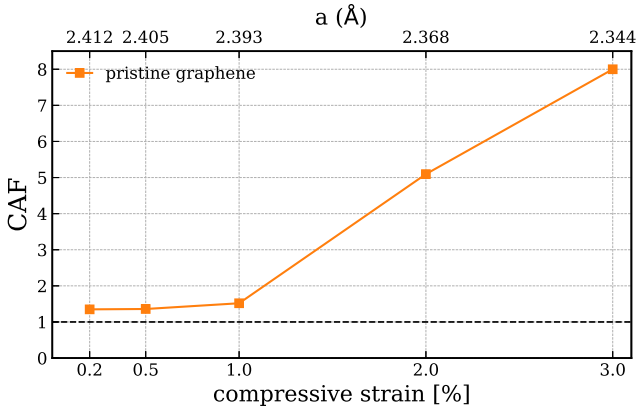

FIG. S11. CAF for compressed pristine graphene on alumina.

Alt text: The plot shows the corrugation amplification factor (CAF) for compressed pristine graphene on alumina as a function of strain. The CAF monotonically increases with increasing compressive strain, reaching a value of 8 at 3% compressive strain.

[1]P. Giannozzi, S. Baroni, N. Bonini, M. Calandra, R. Car, C. Cavazzoni, D. Ceresoli, G. L. Chiarotti, M. Cococcioni, I. Dabo, A. Dal Corso, S. de Gironcoli, S. Fabris, G. Fratesi, R. Gebauer, U. Gerstmann, C. Gougoussis, A. Kokalj, M. Lazzeri, L. Martin-Samos, N. Marzari, F. Mauri, R. Mazzarello, S. Paolini, A. Pasquarello, L. Paulatto, C. Sbraccia, S. Scandolo, G. Sclauzero, A. P. Seitsonen, A. Smogunov, P. Umari, and R. M. Wentzcovitch, "QUANTUM ESPRESSO: a modular and open-source software project for quantum simulations of materials," J. Phys.: Condens. Matter **21**, 395502 (2009).
[2]P. Giannozzi, O. Andreussi, T. Brumme, O. Bunau, M. Buongiorno Nardelli, M. Calandra, R. Car, C. Cavazzoni, D. Ceresoli, M. Cococcioni, N. Colonna, I. Carnimeo, A. Dal Corso, S. de Gironcoli, P. Delugas, R. A. DiStasio, A. Ferretti, A. Floris, G. Fratesi, G. Fugallo, R. Gebauer, U. Gerstmann, F. Giustino, T. Gorni, J. Jia, M. Kawamura, H.-Y. Ko, A. Kokalj, E. Küçükbenli, M. Lazzeri, M. Marsili, N. Marzari, F. Mauri, N. L. Nguyen, H.-V. Nguyen, A. Otero-de-la Roza, L. Paulatto, S. Poncé, D. Rocca, R. Sabatini, B. Santra, M. Schlipf, A. P. Seitsonen, A. Smogunov, I. Timrov, T. Thonhauser, P. Umari, N. Vast, X. Wu, and S. Baroni, "Advanced capabilities for materials modelling with Quantum ESPRESSO," J. Phys.: Condens. Matter **29**, 465901 (2017).
[3]P. Giannozzi, O. Baseggio, P. Bonfà, D. Brunato, R. Car, I. Carnimeo, C. Cavazzoni, S. de Gironcoli, P. Delugas, F. Ferrari Ruffino, A. Ferretti, N. Marzari, I. Timrov, A. Urru, and S. Baroni, "Quantum ESPRESSO toward the exascale," J. Chem. Phys. **152**, 154105 (2020).
[4]G. Prandini, A. Marrazzo, I. E. Castelli, N. Mounet, and N. Marzari, "Precision and efficiency in solid-state pseudopotential calculations," npj Computational Materials **4** (2018), 10.1038/s41524-018-0127-2.
[5]D. Vanderbilt, "Soft self-consistent pseudopotentials in a generalized eigenvalue formalism," Phys. Rev. B **41**, 7892–7895 (1990).
[6]E. Kucukbenli, M. Monni, B. I. Adetunji, X. Ge, G. A. Adebayo, N. Marzari, S. de Gironcoli, and A. D. Corso, "Projector augmented-wave and all-electron calculations across the periodic table: a comparison of structural and energetic properties," (2014), arXiv:1404.3015 [cond-mat.mtrl-sci].
[7]A. Dal Corso, "Pseudopotentials periodic table: From H to Pu," Computational Materials Science **95**, 337–350 (2014).
[8]J. P. Perdew, K. Burke, and M. Ernzerhof, "Generalized Gradient Approximation Made Simple," Phys. Rev. Lett. **77**, 3865–3868 (1996).
[9]S. Grimme, J. Antony, S. Ehrlich, and H. Krieg, "A consistent and accurate ab initio parametrization of density functional dispersion correction (dft-d) for the 94 elements h-pu," The Journal of Chemical Physics **132**, 154104 (2010).
[10]J. I. Hütner, A. Conti, D. Kugler, F. Mittendorfer, G. Kresse, M. Schmid, U. Diebold, and J. Balajka, "Stoichiometric reconstruction of the Al_2O_3 (0001) surface," Science **385**, 1241–1244 (2024).
[11]A. Marmier and S. C. Parker, "Ab initio morphology and surface thermodynamics of $\alpha - Al_2O_3$," Phys. Rev. B **69**, 115409 (2004).
[12]D. Acharya, D. Perilli, and C. Di Valentin, "Optimizing the graphene/$\alpha - Al_2O_3$(0001) interface through minimization of interfacial stress for improved electronic applications," ACS Appl. Nano Mater. **8**, 22626–22636 (2025).
[13]S. Ou, J. E. Heimann, and J. W. Bennett, "A Density Functional Theory (DFT) Investigation of Sulfur-Based Adsorbate Interactions on Alumina and Calcite Surfaces," Clays Clay Miner. **70**, 370–385 (2022).
[14]B. Ramogayana, D. Santos-Carballal, K. P. Maenetja, N. H. de Leeuw, and P. E. Ngoepe, "Density Functional Theory Study of Ethylene Carbonate Adsorption on the (0001) Surface of Aluminum Oxide α-Al_2O_3," ACS Omega **6**, 29577–29587 (2021).
[15]A. Biaggne, G. Noble, and L. Li, "Adsorption and Surface Diffusion of Metals on α-Al_2O_3 for Advanced Manufacturing Applications," JOM **73**, 1062–1070 (2021).
[16]R. Storn and K. Price, "Differential evolution – a simple and efficient heuristic for global optimization over continuous spaces," J. Glob. Optim. **11**, 341–359 (1997).
[17]P. Lazić, "Cellmatch: Combining two unit cells into a common supercell with minimal strain," Comput. Phys. Commun. **197**, 324–334 (2015).
[18]P. Vashishta, R. K. Kalia, A. Nakano, and J. P. Rino, "Interaction potentials for alumina and molecular dynamics simulations of amorphous and liquid alumina," J. Appl. Phys. **103**, 083504 (2008).
[19]S. J. Stuart, A. B. Tutein, and J. A. Harrison, "A reactive potential for hydrocarbons with intermolecular interactions," J. Chem. Phys. **112**, 6472–6486 (2000).
[20]J. Beránek, A. Böhm, G. Palermo, J. Martinovič, and B. Jansík, "Hyperqueue: Efficient and ergonomic task graphs on hpc clusters," SoftwareX **27**, 101814 (2024).
[21]N. A. Mehta, D. A. Levin, V. J. Murray, and T. K. Minton, "Study of non-reactive scattering from graphene using molecular beam experiments and molecular dynamics," AIP Conf. Proc. **1786**, 100003 (2016).
[22]S. Cajahuaringa, D. L. Z. Caetano, L. N. Zanotto, G. Araujo, and M. S. Skaf, "Massccs: A high-performance collision cross-section software for large macromolecular assemblies," J. Chem. Inf. Model **63**, 3557–3566 (2023).
[23]P. Spijker, A. J. Markvoort, P. A. J. Hilbers, S. V. Nedea, and T. Abe, "Velocity correlations and accommodation coefficients for gas-wall interactions in nanochannels," in *AIP Conf. Proc.* (AIP, 2008) pp. 659–664.
[24]F. L. Thiemann, P. Rowe, A. Zen, E. A. Müller, and A. Michaelides, "Defect-dependent corrugation in graphene," Nano Lett. **21**, 8143–8150 (2021).